Article:

Liu, J, Qu, W, Nikitas, N orcid.org/0000-0002-6243-052X et al. (1 more author) (2018) Research on extending the fatigue life of railway steel bridges by using intelligent control. Construction and Building Materials, 168. pp. 532-546. ISSN 0950-0618

https://doi.org/10.1016/j.conbuildmat.2018.02.125

Research on extending the fatigue life of railway steel bridges by using intelligent control

Jia Liu [1*], Weilian Qu [1], Nikolaos Nikitas [2*], Zeliang Ji [3]

1. Hubei Key Laboratory of Roadway Bridge and Structure Engineering, Wuhan University of Technology, Wuhan 430070, China;

2. School of Civil Engineering, University of Leeds, Leeds, LS2 9JT, UK;

3. School of Civil Engineering and Architecture, Wuhan University of Technology, Wuhan 430070, China

Abstract: This paper investigates the potential of a vibration control-inspired method towards extending the fatigue life of railway steel bridges. Based on coupled thermal-mechanical and vehicle-track analysis, both the residual stresses from welding and these from traffic on the bridge are obtained. Subsequently, a multi-scale approach with a shell Finite Element (FE) model of the whole bridge and a solid FE model of its critical joints is put forward. The equation of motion is established for the controlled bridge, equipped with a Magnetorheological-Tuned Mass Damper (MR-TMD) system, while the combination of excitation, welding and control effects is practiced through own-developed packages and commercial software sub-model routines. The framework is showcased for the study of the Poyang Lake Railway Bridge in China. After obtaining the controlled stress states at the critical welded joint, the fatigue crack initial life is evaluated by using the critical plane method and the linear cumulative damage theory. Simulation results indicate that the multi-scale modelling approach followed, meets the accuracy needs for capturing the cracking process of the welded joint with high computational efficiency. The MR-TMD system, even when moderately reducing the critical joint stress amplitudes, can improve substantially the overall bridge fatigue resistance over the uncontrolled structure.

Keywords: Sub-model/multi-scale method; railway steel bridges; fatigue; structural control.

Notation

Section 2.1

k_x	the x directional thermal conductivity factors
k_y	the y directional thermal conductivity factors
k_z	the z directional thermal conductivity factors
λ	efficiency of the heat source
U_w	welding voltage
I_w	welding current
V_H	volume of the welding unit
ρ	the parent material density
C	specific heat capacity
T	the joint temperature generated by the welding
t	the independent time variable
N_x	the perpendicular to the boundary of x direction cosines
N_y	the perpendicular to the boundary of y direction cosines
N_z	the perpendicular to the boundary of z direction cosines
h_c	the heat transfer coefficient of convection
h_r	the heat transfer coefficient of radiation
q_s	boundary heat flux
T_r	temperature of radiation
T_∞	surrounding temperature
f_f	the heat source distribution of the double ellipsoid model for front heat source
f_r	the heat source distribution of the double ellipsoid model for rear heat source
q_f	the heat source of the double ellipsoid model for front heat source
q_r	the heat source of the double ellipsoid model for front heat source
v	welding speed
x_0	the x coordinate of the welding initial position
a_1	arc welding parameter
a_2	arc welding parameter
b	arc welding parameter
c	arc welding parameter
$\{d\sigma\}$	vector of stress
$\{d\varepsilon\}$	vector of strain
dT	temperature increment
$[D]$	elastic or elastic-plastic constitutive law matrix
$\{C\}$	temperature dependence vector

M_c	weight of the train car
J_c	inertia of the train car
M_t	weight of bogies
J_t	inertia of bogies
M_{wi}	the wheel's weight
v_{wi}	vertical displacement of each wheel
v_{ti}	vertical displacement of the bogies
φ_{ti}	rotation angle of the bogies
v_c	vertical displacement of the repeating train car
φ_c	rotation of the repeating train car
u_1, u_2	the rail vertical displacements
u_3, u_4	the railway bridge sleeper vertical displacements
u_5, u_6	the ballast vertical displacement
k_{y1}	the elastic coefficients of the fastener
k_{y2}	the elastic coefficients of the ballast
k_{y3}	the elastic coefficients of the railway bridge sleeper
c_{y1}	the damping coefficients of again the fastener
c_{y2}	the damping coefficients of again ballast
c_{y3}	the damping coefficients of again the railway bridge sleeper
$\mathbf{M_v}$	the mass matrices of the train
$\mathbf{C_v}$	the damping matrices of the train
$\mathbf{K_v}$	stiffness matrices of the train
$\ddot{\mathbf{a}}_\mathbf{v}$	the acceleration vector
$\dot{\mathbf{a}}_\mathbf{v}$	the velocity vector
$\mathbf{a_v}$	the displacement vector
$\mathbf{Q_V}$	the force vector
$\mathbf{M_l}$	the mass, damping vector of the track
$\mathbf{C_l}$	the damping vector of the track
$\mathbf{K_l}$	the stiffness matrices vector of the track
$\mathbf{Q_l}$	the load vector of the track
e	the element identifier of the 2D track beam
k_H	the equivalent spring stiffness
u_i	the interpolating function of u_1 and u_2 of the nodal displacement
$\mathbf{M}_C$	the mass matrices of the coupled system
$\mathbf{C_C}$	the damping matrices of the coupled system
$\mathbf{K_C}$	the stiffness matrices of the coupled system
$\mathbf{Q_C}$	the load vector
$\mathbf{C_{Vl}}, \mathbf{C_{lV}}$	the coupling damping
Ω	spatial angular frequency variable

Ω_c	the truncated spatial angular frequency of the vertical profile irregularity
Ω_r	the truncated spatial angular frequency of the alignment irregularity
A_v	the high interference roughness coefficient

Section 3.1

Z_r , Z	the vertical displacements of the bridge deck and TMD mass respectivelly
$\ddot{\mathbf{x}}$	the acceleration vector of the bridge discrete model
$\dot{\mathbf{x}}$	the velocity vector of the bridge discrete model
$\mathbf{x}$	the displacement vector of the bridge discrete model
M	the mass matrices
C	the stiffness matrices
K	the damping matrices
H	locator matrix of installed MR-TMD system
F(t)	the external force input
$\mathbf{U}_{\text{MR-TMD}}$	the control force vector provided by the MR-TMD system
K_{Ti}	the stiffness properties of the i^{th} TMD in the MR-TMD
C_{Ti}	the damping properties of the i^{th} TMD in the MR-TMD
F_{MRi}	the damping force of the i^{th} MR damper
C_d	the viscous damping coefficient
F_d	the coefficient of controllable Coulomb damping force
K_d	the equivalent axial stiffness of the damper
f_{0i}	the output force deviation caused by the damper accumulator
e_b	the Bingham sliding displacement
C_{ds}	the coefficient of viscous damping of damper on the condition of zero electric field strength
F_{ds}	the coefficient of controllable Coulomb damping force of damper on the condition of zero electric field strength
K_{ds}	the equivalent axial stiffness of damper on the condition of zero electric field strength
C_{dd}	the voltage sensitivity of viscous damping of the damper
F_{dd}	the voltage sensitivity of controllable Coulomb damping force of the damper
K_{dd}	the voltage sensitivity of equivalent axial stiffness of the damper
η	the time coefficient of the damper's magnetic hysteresis response
I	the applied current intensity
u	the internal variable reflecting the relationship between model parameters and current intensity.

Section 3.2

$F_{d\,max}$	the maximum coefficient
$F_{d\,min}$	the minimum coefficient
ξ	the adjustment factor of the Coulomb damping force

Section 3.4

ε_x	the x-directional normal strain
ε_y	the y-directional normal strain
ε_z	the z-directional normal strain
ε_{xy}	the xz-directional shear strain
ε_{yz}	the yz-directional shear strain
ε_{xz}	the xz-directional shear strain
$\varepsilon_{z'z'}$, $\varepsilon_{x'z'}$, $\varepsilon_{y'z'}$	the intermediate step calculation parameters
θ, Φ	the calculated angles
$\Delta\varepsilon_{eq}^{cr}$	the multi-axis fatigue damage parameter of equivalent strain
ε_n^*	the normal strain amplitude obtained by the cycle counting
$\Delta\gamma_{max}$	the relevant shear strain amplitude
$\Delta\varepsilon_a$	the total strain amplitude
$\Delta\varepsilon_e$	the elastic strain amplitude
$\Delta\varepsilon_p$	the plastic strain amplitude
$\sigma_f^{'}$	the fatigue strength coefficient
$\varepsilon_f^{'}$	the fatigue plastic coefficient
E	the material elastic modulus
m	the elastic fatigue strength index
n	the plastic fatigue strength index
N_f	the cycle counts of fatigue life
σ_m	the average stress
$\overline{\sigma_m}$	the mean value of calculated redistributed welding residual stress
σ_s	the yield strength of steel
D=1	the critical failure fatigue threshold

1. Introduction

Railway steel bridges are very common long span bridges, constituting a large sector of the traffic communication network. Owing to their long time and frequent train traffic, cumulative damage may occur in their welded regions. In particular, stress concentrations can easily be generated under the combined action of multi-axial dynamic-excitation stress and welding-owed residual stress. Such could further lead to fatigue damage that sets off as crack initiation and, in a worst case scenario, could progress to failure of parts of the bridge, putting a serious concern in terms of life cycle design. Collapse and damage of steel bridges caused by cumulative fatigue action have been frequently reported across the world up to this date [1-3]. Therefore, it is important to propose and adopt effective means to prolong the fatigue crack initial life of steel bridge parts; such could subsequently extend the service life of railway steel bridges, and reduce the risk, economic losses and casualties caused by potential damage.

In the past decades, many scholars have carried out considerable theoretical and experimental research in the field of bridge fatigue life assessment. Namely, within the achievements produced in the field one can quote the establishment of fatigue damage models, the study of initial crack mechanisms and the evaluation of a structure’s overall fatigue life [4,5]. Li and Chan, for instance, applied continuous damage mechanics to their dynamic constitutive model, and combining modelling with strain measurements from a state-of-the-art online health monitoring system, evaluated the fatigue life of the Tsing Ma Bridge under vehicle vibration [6]. Xu et al. established a fatigue damage evolution model based on continuous damage mechanics, and evaluated the fatigue life of the key steel parts of the Tsing Ma Bridge under wind load according to the so-called hot spot stress [7]. Guo et al. researched the effect of environmental temperature on the fatigue life of the welded steel bridge deck of the Runyang Suspension Bridge, finding that the relationship between temperature and fatigue life of welded nodes is linear within a certain temperature range [8]. Righiniotis studied the fatigue life of railway steel bridges under increasing train traffic load, and concluded that when the train load increased to a certain degree, the fatigue life was drastically reduced [9].

However, little of the literature addressed pathways to extend the fatigue life of steel bridges, and particularly the research which adopts intelligent control techniques to do so for railway applications is relatively sparse. Thus, a method is herein proposed to mitigate the responses of civil engineering structures and reduce the stress cycle amplitudes by using a Magnetorheological - Tuned Mass Damper (MR-TMD) control system. It is well known that TMDs can mitigate the vertical responses in the middle span of a bridge without auxiliary supporting structures and with minimal aesthetic intrusion to the architectural shape. Besides, MR dampers are among the most promising control devices that can adjust in an active fashion the provided damping force in order to yield increased vibration mitigation performance. In addition, there are many relevant studies on the use of intelligent materials, intelligent configurations, and intelligent algorithms [10-12]. For the case of a pedestrian bridge, that vibration monitoring showed prone to human-induced vibrations, Caetano et al. proposed an effective TMD control system and demonstrated experimentally the effectiveness of it [13]. Closer to the railway and fatigue focus of this paper, Andersson et al. developed a procedure to account for detuning effects associated with passive TMD systems of train-loaded bridges. Using an incremental frequency estimation technique for adjusting a variable stiffness TMD, they researched numerically the cumulative fatigue damage on a case study bridge equipped with different mass damper systems, ultimately establishing that adaptive systems can significantly outperform passive equivalents [14]. Museros et al. researched the control effect on moving loads' dynamic stresses for a simply supported girder bridge when using viscous fluid dampers [15]. The same research team further proposed the potential of extending their methodology to applications of railway bridges, and indeed two railway bridges in Spain were theoretically studied using this method, obtaining excellent vibration/stress control performance [16]. Wang et al. researched the classical problem of defining optimal parameters for a TMD, presenting an optimisation technique for a steel railway bridge under different train traffic scenarios. For the underlying numerical analysis of their TMD's control efficiency, they considered parameters such as the static displacement of the bridge middle span, the TMD's mass block expenditure and the difficulty of the damper manufacturing [17]. Luu et al., similarly on optimisation grounds, presented a method where the TMD system parameters are directly tuned based on an objective function taking into account the H2 norm and the constraints of all peaks of the same height over the frequency range of interest. The result is multi-modal, robust vibration control directly applicable to multi-span railway bridges [18]. Younesian et al. beyond studying the optimal frequency and damping ratio of a TMD system, also attempted to uncover the effect of boundary conditions on TMD performance for the indicative case of a Timoshenko beam [19]. Kahya et al. designed a series multiple tuned mass damper (STMD) device consisting of two in series connected spring-mass-damper units. The assembly was shown that can effectively suppress the resonance introduced from high-speed trains (HSTs), being at the same time economical and sufficiently robust to detuning effects [20]. Yau proposed a string-type tuned mass damper composed of a distributed TMD subsystem and a stretched string acting on a simple beam. The outcome for this ensemble is a TMD with an adjustable tuning frequency, which could more efficiently mitigate resonant response due to moving loads [21]. Lin et al. numerically studied the effect of multiple tuned mass dampers (MTMDs) on the suppression of train vibrations on real Taiwan High Speed

Rail (THSR) bridges. For the narrow band train traffic loads they recovered that MTMDs are more effective, robust and reliable than a single passive TMD not only at resonance speeds but throughout the operational range [22].

This paper also concentrates on a method to dynamically control, in practice, railway bridges for subsequently extending the fatigue crack initial life of their welded joints. Based on coupled thermal-mechanical and vehicle-track theories, the residual stresses, owing to welding, and the dynamic train traffic actions exerted on the joints of the bridge are respectively obtained. A multi-scale FE shell model of the whole railway steel bridge and a FE solid model of its critical joint in the middle span have been set up jointly based on a sub-model realisation. Further, the equation of motion for the controlled bridge installed with a MR-TMD apparatus is established. The whole approach together with the required control force estimation is practiced by using a commercial software sub-model solution and enriched by own routines. The Poyang Lake Railway Bridge in China has become the testbed of the developed analytical framework. After recovering the controlled stress states in the most critical welded joint location, the fatigue crack initial life is evaluated by using the critical plane method and the linear cumulative damage theory.

2. Simulation method for accurate joint stress calculations

In order to evaluate the fatigue crack initial life of the bridge, it is essential to obtain the accurate stress response of its welded joints. In this section, the simulation principle for evaluating the welding residual stresses and the train traffic load is presented. Further, towards the accurate stress modelling for the bridge joints, the sub-model interaction proposed is described.

2.1 Load simulation

2.1.1 Simulation of welding residual stress

The simulation of the welding residual stress on the joints of the steel bridge is practised in two steps: In the first step, the double ellipsoidal heat source model [23] is used to calculate the real-time temperature fields in the welded area while using the actual welding parameters, and also taking into account the cooling process. In the second step, the recovered temperature fields are applied as external loads to the mechanical model of the joint, and the real-time stress field in the welded area is produced. The stress of the joint, after also cooling has elapsed, is taken forward in the analysis as the welding residual stress [24-26].

Indicatively the steps go as follows. The transient nonlinear heat conduction differential equation for the welding process can be expressed as [27]:

$$\frac{\partial}{\partial x}(k_x \frac{\partial T}{\partial x}) + \frac{\partial}{\partial y}(k_y \frac{\partial T}{\partial y}) + \frac{\partial}{\partial z}(k_z \frac{\partial T}{\partial z}) + Q = \rho C \frac{\partial T}{\partial t} \tag{1}$$

where k_x, k_y and k_z are the x, y and z directional thermal conductivity factors, respectively; $Q = \lambda U_w I_w / V_H$ is the heat generation rate, λ is the efficiency of the heat source, U_w and I_w are respectively the welding voltage and current, V_H is the volume of the welding unit; ρ and C are the parent material density and specific heat capacity, T is the joint temperature generated by the welding and t is the independent time variable.

The initial value and boundary conditions of Eq. (1) are:

$$T(x, y, z, 0) = T_0(x, y, z) \tag{2}$$

$$k_x \frac{\partial T}{\partial x} N_x + k_y \frac{\partial T}{\partial y} N_y + k_z \frac{\partial T}{\partial z} N_z + q_s + h_c(T - T_\infty) + h_r(T - T_r) = 0 \tag{3}$$

where N_x, N_y and N_z are the perpendicular to the boundary of each direction cosines, h_c and h_r are the heat transfer coefficient of convection and radiation respectively, q_s is the boundary heat flux, T_r denotes the temperature of radiation; and T_∞ represents the surrounding temperature.

The functions of the double ellipsoidal heat source model can be expressed as [23]:

Front heat source

$$q_f(x,y,z,t)=\frac{6\sqrt{3}f_fQ}{a_1bc\pi\sqrt{\pi}}e^{-3(x-vt-x_0)^2/a_1^2}e^{-3y^2/b^2}e^{-3z^2/c^2} \quad (4)$$

Rear heat source

$$q_r(x,y,z,t)=\frac{6\sqrt{3}f_rQ}{a_2bc\pi\sqrt{\pi}}e^{-3(x-vt-x_0)^2/a_2^2}e^{-3y^2/b^2}e^{-3z^2/c^2} \quad (5)$$

where f_f and f_r are the heat source distribution of the double ellipsoid model for either front or rear heat source, $f_f + f_r=2$; q_f and q_r are the heat source of the double ellipsoid model for either front or rear heat source; v is the welding speed; x_0 is the x coordinate of the welding initial position and a_1, a_2, b and c are arc welding parameters.

The Von Misses yield criterion is used to simulate the real-time stress fields [17]:

$$\{d\sigma\}=[D]\{d\varepsilon\}-\{C\}dT \quad (6)$$

where $\{d\sigma\}$ and $\{d\varepsilon\}$ are the vectors of stress and strain, respectively; and dT is the temperature increment, $[D]$ is the elastic or elastic-plastic constitutive law matrix and $\{C\}$ is the temperature dependence vector.

2.1.2 Simulation of train traffic load

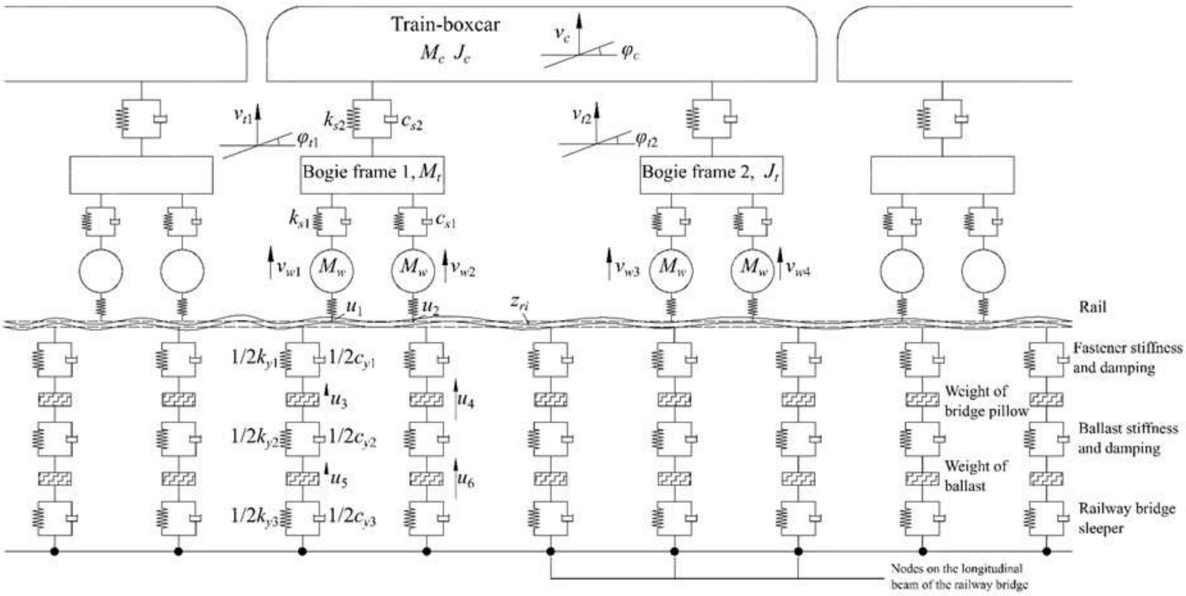

Fig.1 Vehicle-track dynamic coupling model

Based on rigid body kinematics, the vehicle-track dynamic coupling model is established to simulate the whole process of a train crossing the bridge [28]. Any interaction effect between the vibration response of the bridge and the track-vehicle system loads is not considered in the paper. The vehicle-track dynamic coupling model is shown in Fig.1. As it is depicted, M_c and J_c are the weight and inertia of the train car, M_t and J_t are the weight and inertia of bogies, $M_{wi}(i=1,2,3,4)$ are the wheel's weight, $v_{wi}(i=1,2,3,4)$ are the vertical displacement of each wheel; $v_{ti}(i=1,2)$ and $\varphi_{ti}(i=1,2)$ are the vertical displacement and rotation angle of the bogies, v_c and φ_c are the vertical displacement and rotation of the repeating train car, u_1 and u_2 are the rail vertical displacements, u_3 and u_4 are the railway bridge sleeper vertical displacements, u_5 and u_6 are the ballast vertical displacement; k_{y1}, k_{y2} and k_{y3} are the elastic coefficients of the fastener, ballast and railway bridge sleeper respectively, and c_{y1}, c_{y2} and c_{y3} are the damping coefficients of again the fastener, ballast and railway bridge sleeper respectively.

The train motion equation is established based on a Lagrangian formulation [29]:

$$\mathbf{M_v\ddot{a}_v + C_v\dot{a}_v + K_v a_v = Q_v} \tag{7}$$

where $\mathbf{M_v}$, $\mathbf{C_v}$ and $\mathbf{K_v}$ are the mass, damping and stiffness matrices of the train, respectively, $\mathbf{\ddot{a}_v}$, $\mathbf{\dot{a}_v}$ and $\mathbf{a_v}$ are the acceleration, velocity and displacement vectors respectively, and $\mathbf{Q_v}$ is the force vector.

For the track model, the motion equation of the track can be obtained by using the three layers of the mass-spring-damper elastic system with discrete supports based on the Hamilton principle [29]:

$$\mathbf{M_l\ddot{a}_l + C_l\dot{a}_l + K_l a_l = Q_l} \tag{8}$$

In which $\mathbf{M_l} = \sum[\mathrm{m}]^e$, $\mathbf{C_l} = \sum[\mathrm{c}]^e$, $\mathbf{K_l} = \sum[\mathrm{k}]^e$ and $\mathbf{Q_l} = \sum[\mathrm{Q}]^e$ are the mass, damping, stiffness matrices and load vector of the track, respectively; e is the element identifier of the 2D track beam.

The $\mathbf{Q_v}$ and $\mathbf{Q_1}$ load vectors in Eqs.(7) and (8) are functions of the wheel displacement v_{wi}, the track node displacements u_1, u_2 and the track irregularity z_{ri}. Their elements can be expressed as:

$$Q_{vi} = f_1(v_{wi}, u_{1i}, u_{2i}, z_{ri}) = k_H(v_{wi} - u_i - z_{ri}) \tag{9}$$

$$Q_{li} = f_2(v_{wi}, u_{1i}, u_{2i}, z_{ri}) = -k_H(v_{wi} - u_i - z_{ri}) \tag{10}$$

According to the Hertz contact theory, the contact between wheel and rail is simplified to linear elastic, where k_H is taken as the equivalent spring stiffness for it. The displacement u_i of the track element can be expressed by the interpolating function of u_1 and u_2 of the nodal displacement [29].

Finally, the vehicle-track coupling dynamic equation is established as:

$$\mathbf{M_C\ddot{a} + C_C\dot{a} + K_C a = Q_C} \tag{11}$$

where $\mathbf{M}_C = \begin{bmatrix} \mathbf{M_v} & \mathbf{0} \\ \mathbf{0} & \mathbf{M_l} \end{bmatrix}$, $\mathbf{C}_C = \begin{bmatrix} \mathbf{C_v} & \mathbf{C_{vl}} \\ \mathbf{C_{lv}} & \mathbf{C_l} \end{bmatrix}$ and $\mathbf{K}_C = \begin{bmatrix} \mathbf{K_v} & \mathbf{K_{vl}} \\ \mathbf{K_{lv}} & \mathbf{K_l} \end{bmatrix}$ are respectively the mass, damping and stiffness matrices of the coupled system; $\mathbf{Q_C} = \begin{Bmatrix} \mathbf{Q_v} \\ \mathbf{Q_l} \end{Bmatrix}$ is the load vector; $\mathbf{C_{Vl}}$ and $\mathbf{C_{lV}}$ are the coupling damping, with $\mathbf{C_{Vl}} = \mathbf{C_{lV}}$, and $\mathbf{K_{Vl}}$ and $\mathbf{K_{lV}}$ are the coupling stiffness matrix block elements with $\mathbf{K_{Vl}} = \mathbf{K_{lV}}$; their calculation can be practiced as in previous cases [29].

The train passage time-history on the railway is simulated by using the German [28] high interference track irregularity power spectrum density function as provided for freight railway lines. For the cases of this study, the vertical irregularity power spectral density function of the line is expressed by the formula:

$$S_v(\Omega) = \frac{A_v \cdot \Omega_c^2}{\left(\Omega^2 + \Omega_r^2\right)\left(\Omega^2 + \Omega_c^2\right)} \tag{12}$$

where Ω is the spatial angular frequency variable, Ω_c is the truncated spatial angular frequency of the vertical profile irregularity, Ω_r is the truncated spatial angular frequency of the alignment irregularity, and A_v is the high interference roughness coefficient.

Employing a step-by-step integration scheme, the real time-history curve of forces on the rail nodes at any instant is produced. This can subsequently be considered as the load on the full-bridge shell FE model scrutinised in the next section.

2.2 Accurate overall stress response evaluation

In order to obtain the accurate stress response of the welded joints of a railway steel bridge, a good insightful numerical model is compulsory for all calculation and analysis purposes. On the one hand, the welding residual stresses are mainly related to the distribution of the welding seam, so a fine solid model should be used to analyse them. On the other hand, the train traffic load is more related to the joint position on the full bridge. Thus, a single solid joint model is not practical to employ for establishing the dynamic responses caused by train traffic. Besides, if a solid FE model was to use for the full bridge, the complexity level would be too high to make practical and the overall numerical efficiency would be classed as low. In order to get a balance between output accuracy and analytical efficiency, a multi-scale modelling approach based on the sub-model method is adopted [30]. The sub-model method is a detached modelling practice based on Saint-Venant's principle, also called as the cutting boundary displacement method. The displacements and loads on the corresponding sub-model boundary of the “coarse” shell full-bridge model are extracted and applied to the relatively fine solid sub-model of the bridge joint; this is seen as the best practical compromise.

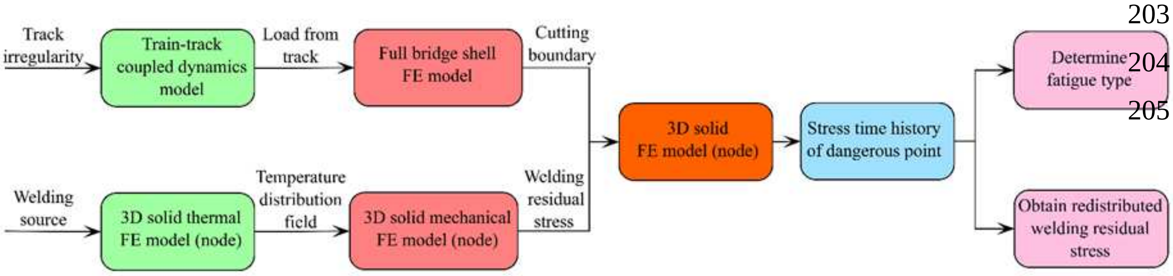

Fig.2 Flow chart to obtain the stress response of railway steel bridge nodes

Fig.2 shows the flow chart for obtaining the stress response of the railway steel bridge joints. According to the vehicle-track coupling dynamics model, mentioned above, the train traffic loads acting on the nodes along the bridge are obtained by using the track irregularity as excitation. These are to be applied on the full-bridge shell FE model. Subsequently, the dynamic boundary responses of the shell full-bridge model in the position of the corresponding solid joint sub-model can be extracted. Meanwhile, the distribution of the welding residual stresses in the joints are captured through the thermal-mechanical fine solid model, which is acted by the same heat source of the actual welding process. The variation within the temperature fields are recorded at both rising and cooling temperatures and the residual stress maps can be obtained from the fine thermal solid model when exposing it to the recorded temperature fields. The boundary conditions of the solid model in the corresponding position of the shell model are applied as external loads while the welding residual stresses are input too within the fine solid model. Consequently, the accurate dynamic stress history of the examined joint within the railway steel bridge when considering the combined welded residual stress and train traffic loads is calculated. The data recovered can be used to estimate the overall fatigue life depending on whether the maximum combined stress will exceed the yield threshold. If it does, the stress fatigue analysis method can be used for subsequent estimations, otherwise the strain fatigue procedure is opted for. Additionally, the welding residual stresses will be released under the external stimulus [31], allowing the process to also uncover the redistributed welded stresses values.

3. Intelligent control towards extending fatigue crack resistance

It is well known that the cumulative fatigue damage of railway steel bridges is mainly induced by cyclic stresses under train running loads. Reducing the amplitude of the cyclic stress by vibration control can evidently improve the fatigue crack resistance of such a bridge. Among all the control devices, the MR damper is probably the most promising intelligent control device being popular for vibration mitigation in civil engineering structures due to its quick response, low energy consumption and good control performance [32]. On similar practicality-performance grounds, TMDs are ideal for bridges because of their limited support needs, their many installations' experience, and their non-aesthetically intrusive character. Therefore, a combined MR-TMD intelligent control system is chosen in this remedy for controlling the cyclic stressing behaviour in order to extend the overall structural fatigue life.

3.1 MR-TMD equipped bridge; the controlled model

Due to the maximum dynamic response generated in the middle span of the railway steel bridge, when loaded by train traffic, the MR-TMD system is more effective to set up in the middle span. Fig.3 schematically depicts the bridge mechanical model with the MR-TMD in place. Assuming that vertical displacement of the bridge deck and the vertical displacement of the MR-TMD auxiliary mass are Z_r and Z respectively, the equation of motion for the bridge can be expressed as:

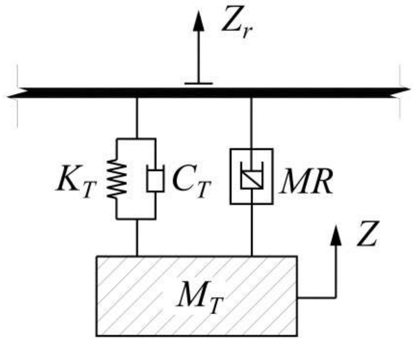

Fig.3 Schematic of the bridge MR-TMD system model

$$\mathbf{M\ddot{x}+C\dot{x}+Kx=F(t)-HU}_{\text{MR-TMD}} \tag{13}$$

where $\mathbf{\ddot{x}}$, $\mathbf{\dot{x}}$ and $\mathbf{x}$ are the acceleration, velocity and displacement vectors of the bridge discrete model, respectively, $\mathbf{M}$, $\mathbf{C}$ and $\mathbf{K}$ are the mass, stiffness and damping matrices, respectively, $\mathbf{H}$ is the locator matrix of the installed MR-TMD system, $\mathbf{F(t)}$ is the external force input, and $\mathbf{U}_{\text{MR-TMD}}$ is the control force vector provided by the MR-TMD system. The latter for an ensemble of MR-TMDs can be expressed as:

$$U_{MR-TMDi} = K_{Ti}\left(Z_{ri} - Z_i\right) + C_{Ti}\left(\dot{Z}_{ri} - \dot{Z}_i\right) + F_{MRi}\left(Z_r - Z, \dot{e}\right) \tag{14}$$

where K_{Ti} and C_{Ti} are the stiffness and damping properties of the i^{th} TMD in the MR-TMD assembly and F_{MRi} is the damping force of the i^{th} MR damper; this can be expressed [33] as:

$$F_{MRi} = C_{di}\dot{e} + F_{di}\,\mathrm{sgn}\left(\dot{e}\right) - f_{0i} = K_{di}\left(Z_r - Z - e\right) - f_{0i} \tag{15}$$

where C_d is the viscous damping coefficient, F_d is the coefficient of controllable Coulomb damping force, K_d is the equivalent axial stiffness of the damper, f_{0i} is the output force deviation caused by the damper accumulator, e_b is the Bingham sliding displacement and sgn designates the sign function. All the C_d , F_d and K_d parameters are related to the system’s current intensity and can be expressed through:

$$\left.\begin{aligned} C_d &= C_{ds} + C_{dd}u \\ F_d &= F_{ds} + F_{dd}u \\ K_d &= K_{ds} + K_{dd}u \end{aligned}\right\} \tag{16}$$

$$\dot{u} = -\eta\left(u - I\right) \tag{17}$$

in which C_{ds}, F_{ds} and K_{ds} are the coefficient of viscous damping, the controllable Coulomb damping force and the equivalent axial stiffness of damper on the condition of zero electric field strength respectively, C_{dd} , F_{dd} and K_{dd} are the voltage sensitivity of viscous damping, controllable Coulomb damping force and equivalent axial stiffness of the damper respectively, η is the time coefficient of the damper's magnetic hysteresis response; the larger the value of η, the shorter the response time, with response time not taken into account explicitly in this paper; I is the applied current intensity, and u is the internal variable reflecting the relationship between model parameters and current intensity. There are eight unknown parameters in the mechanical model $(C_{ds}, F_{ds}, K_{ds}, C_{dd}, F_{dd}, K_{dd}, f_{0i}, \eta)$ which can be defined through parameter identification on actual test results for each MR damper. Performing this step, the mechanical model could be fully established.

3.2 Control algorithm of MR-TMD system

There are many options for the control algorithms to drive the MR damper system. Still, it is not the focus of this paper to research on the control algorithm efficacy. Therefore, the simplest and most practical fixed incremental control solution is adopted; this is abundant in engineering applications. The fixed incremental control algorithm dissipates energy [33] through the limiting condition that when structural displacement and the TMD auxiliary mass velocity are in the same direction, then the adjustable Coulomb force is increased until it reaches the required current; on the contrary when the quoted response quantities are opposite, the adjustable Coulomb force is stepwise reduced until it shuts down. This principal is expressed through:

$$F_d(t+1)=\begin{cases}\min(F_d(t)+\xi F_{d\max},F_{d\max}) & Z_r\cdot\dot{Z}>0\\ \max(F_d(t)\text{-}\xi F_{d\max},F_{d\min}) & Z_r\cdot\dot{Z}\le 0\end{cases} \tag{18}$$

where now $F_{d\max}$, $F_{d\min}$ are the maximum and minimum coefficients and ξ is the adjustment factor of the Coulomb damping force.

3.3 Extending the fatigue crack initial life; the sub-modelling approach

The key to enable improvements for the fatigue crack initial life of a railway steel bridge is to size accurately the dynamic stress response of the critical joint location after installing the MR-TMD control system. However, it is difficult to capture any stress updating directly by using off-the-shelf FE software because of the lack for example of control capabilities within such tools. Additionally, self-developed FE coding using sub-models of details (i.e. refined solid models) are hard to implement and could result in low computational efficiency. To this goal, a self-developed control program in FORTRAN was implemented and was combined to a multi-scale modelling scheme using commercial FE software in order to obtain the bridge critical point stress time-histories. The control model in FORTRAN is extracting sufficient modes from ANSYS in order to use the modal decomposition method for the response and control force calculations. As such, the bridge model in FORTRAN and ANSYS are expected to yield very close results. Fig.4 schematically depicts the methodology towards obtaining the controlled stress time-histories of the bridge with an added dynamic control system on. First, under railway load, the controlled actions and responses are evaluated through a FORTRAN package. These results are then fed as loading boundary input into the full bridge shell model, at the corresponding locations, of a commercial FE suite such as ANSYS. The subsequent calculations extract the controlled response at all bridge boundaries and particularly at the specific boundaries of the critical joint, for which a solid sub-model exists, a record is taken. The controlled stress-time history curve of the solid model is calculated after combining data with the residual welding stress analysis. This information is further used as the basis for evaluating the impact of control interventions on the fatigue crack initial life of the bridge's most critical welded areas.

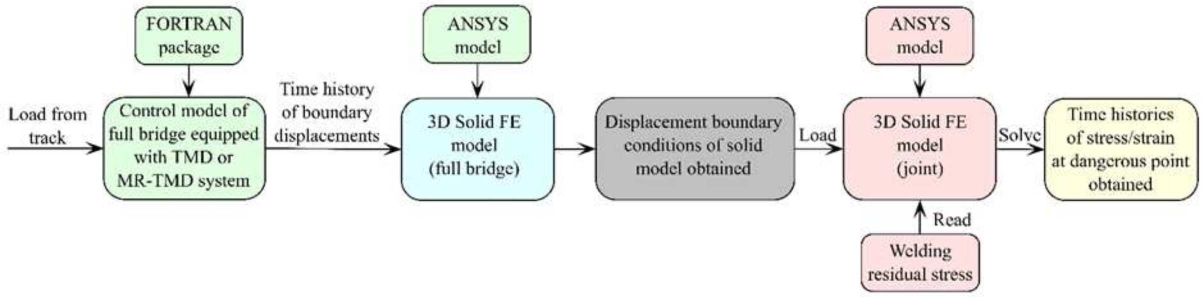

Fig.4 Flow chart for obtaining controlled stress time-history curve

3.4 Estimation of the fatigue crack initial life

Based on the microscopic study of material crack initiation, the critical plane method assumes a damage parameter, which here is the critical shear strain value of the material under cyclic loading. The critical plane coincides with the fatigue crack initial plane of highest risk [5]. Using the six strain time-history curves for the most severely loaded point, obtained in the previous section, the orientation of the critical plane is searched through changing its angular position relative to the reference plane in a step-like manner.

$$\begin{cases} \varepsilon_{z'z'}(\theta,\Phi) = \sin^2\Phi(\varepsilon_x \sin^2\theta + \varepsilon_y \cos^2\theta - \varepsilon_{xy}\sin 2\theta) + 0.5(\varepsilon_{xz}\sin\theta\sin 2\Phi - \varepsilon_{yz}\cos\theta\sin 2\Phi) + \varepsilon_z \cos^2\Phi \\ \varepsilon_{x'z'}(\theta,\Phi) = 0.5(\varepsilon_x - \varepsilon_y)\sin 2\theta\sin\Phi - \varepsilon_{xy}\cos 2\theta\sin\Phi + \varepsilon_{xz}\cos\theta\cos\Phi + \varepsilon_{yz}\sin\theta\cos\Phi \\ \varepsilon_{y'z'}(\theta,\Phi) = 0.5\sin 2\Phi(-\varepsilon_x \sin^2\theta - \varepsilon_y \cos^2\theta + \varepsilon_z + \varepsilon_{xy}\sin 2\theta) - \varepsilon_{xz}\sin\theta\cos 2\Phi + \varepsilon_{yz}\cos\theta\cos 2\Phi \end{cases} \tag{19}$$

where ε_x, ε_y, ε_z are the x, y, z-directional normal strains obtained by ANSYS, ε_{xy}, ε_{yz}, ε_{xz} are the xy, yz, xz-directional shear strains, $\varepsilon_{z'z'}$, $\varepsilon_{x'z'}$, $\varepsilon_{y'z'}$ are the intermediate step calculation parameters and [θ, Φ] are the calculated angles.

Due to the random load, the shear strain and the normal strain on the plane of the material are changing substantially, and they show continuous variation. Thus, a weight function is used to determine the critical plane [33]. Thereafter, the normal and shear strain time-history curves of this critical plane are obtained by:

$$\begin{aligned} &\gamma(\theta',\Phi') = \sqrt{[\varepsilon_{x'z'}(\theta',\Phi')]^2 + [\varepsilon_{y'z'}(\theta',\Phi')]^2} \\ &\varepsilon_n(\theta',\Phi') = \varepsilon_{z'z'}(\theta',\Phi') \end{aligned} \tag{20}$$

In which, γ is the critical plane shear strain, ε_n is the critical plane normal strain and $[\theta',\Phi']$ are the critical interface angles calculated through the weight function method.

Meanwhile, the normal strain amplitude and shear strain amplitude are extracted by using the rain-flow counting method to make all fatigue estimations for the bridge. In order to effectively evaluate the multi-axial fatigue crack initial life, the Von-Mises criterion is adopted to reconfigure the normal and shear strain amplitudes into an equivalent strain amplitude on the critical plane; that is:

$$\Delta\varepsilon_{eq}^{cr}/2 = [\varepsilon_n^{*2} + \frac{1}{3}(\Delta\gamma_{max}/2)^2]^{\frac{1}{2}} \tag{21}$$

where $\Delta\varepsilon_{eq}^{cr}$ is the multi-axis fatigue damage parameter of equivalent stain, ε_n^* is the normal strain amplitude obtained by the cycle counting, and $\Delta\gamma_{max}$ is the relevant shear strain amplitude. The fatigue strain variables include elastic and plastic parts, whereby the total strain can be written as:

$$\Delta\varepsilon_a = \Delta\varepsilon_e + \Delta\varepsilon_p \tag{22}$$

where $\Delta\varepsilon_a$ is the total strain amplitude, $\Delta\varepsilon_e$ is the elastic strain amplitude, and $\Delta\varepsilon_p$ is the plastic strain amplitude. Subsequently, the amplitude of elastic and plastic strains can be expressed respectively by:

$$\frac{\Delta\varepsilon_e}{2} = \frac{\sigma_f'}{E}\left(2N_f\right)^m \tag{23}$$

$$\frac{\Delta\varepsilon_p}{2} = \varepsilon_f'\left(2N_f\right)^n \tag{24}$$

where $\sigma_f^{'}$ is the fatigue strength coefficient, $\varepsilon_f^{'}$ is the fatigue plastic coefficient, E is the material elastic modulus, m and n are the elastic and plastic fatigue strength index, and N_f is the cycle counts of fatigue life.

The fatigue initial life is assessed by the Manson-Conffin formula which considers in unity high cycle and low cycle fatigue [34]. Considering the effect of the welding residual stress on the fatigue life, the average stress σ_m is introduced into the elastic strain, and the elastic fatigue strength coefficient $\sigma_f^{'}$ is modified to $\sigma_f^{'} - \sigma_m$ [35]; this yields the modified Manson-Conffin formula:

$$\frac{\Delta\varepsilon_{eq}^{cr}}{2} = \frac{\sigma_f^{'} - \sigma_m}{E}\left(2N_f\right)^b + \varepsilon_f^{'}\left(2N_f\right)^c \tag{25}$$

where $\sigma_m = \overline{\sigma_m} + 0.3\sigma_s$, $\overline{\sigma_m}$ is the mean value of calculated redistributed welding residual stress, and σ_s is the yield strength of steel.

The number of fatigue life cycles N_f of the railway steel bridge is obtained by substituting the equivalent strain amplitude into Eq.(24), while also the damage degree $D_i = 1 \Big/ \sum_{j=1}^{n} N_{f_j}$ is calculated for when a train crosses the bridge. Based on the Miner linear cumulative damage theory [5], the fatigue crack initial life in any of the welded bridge joints for the combined complex loading – vibration control condition is designated by:

$$D = \sum_{1}^{k} D_i \qquad (i = 1, 2, \ldots k) \tag{26}$$

where k is the number of the train crossing bridge. Assuming that D=1 is used as the critical failure fatigue threshold, if D is greater than 1 fatigue occurs, while if D is less than 1, any fatigue damage is prevented [36].

4. Case study; the Poyang Lake railway bridge

4.1 Bridge background

The Poyang Lake Railway Bridge, is a railway steel truss bridge located at the Tong-Jiu railway freight line in China. The layout of its spans is 4×120 m, totalling 480 m in length. Each span is composed of 10 sections with each having 14.5 m height, 13 m width, and 12 m length, as illustrated in Fig.5, which schematically presents only half of the symmetrical railway truss bridge. The chord member of the truss is of box section with 0.8 m×0.8 m size. The material of the web member, the vertical and horizontal beam and the upper and lower flat of the truss is H-steel. In addition, the lower joint in the first span is 3.5 m long, 1.5 m high, and has a plate thickness of 0.04 m. The joint is a welded integral joint with four fillet welds and each member is connected to it by bolts as shown in the detailed joint diagram inset to Fig.5.

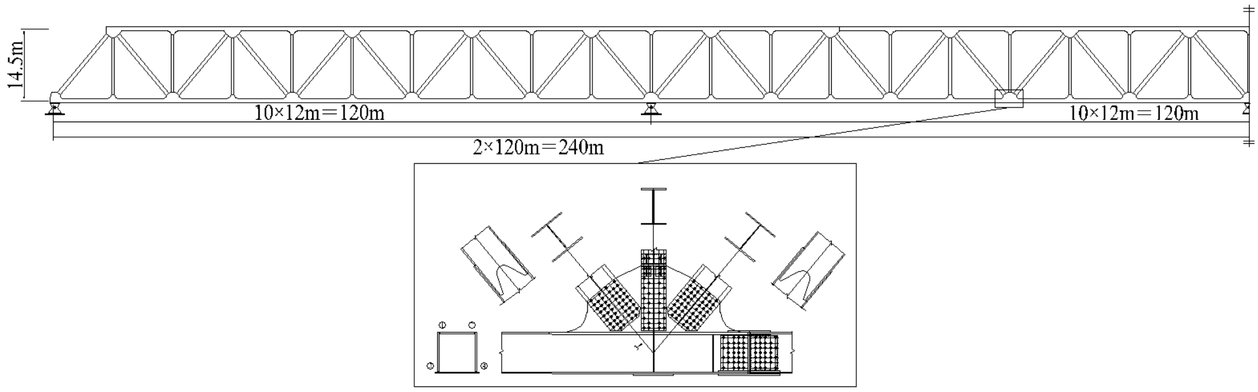

Fig.5 The schematic diagram of railway bridge structure

4.2 Multi-scale FE modelling of the bridge

For any complex civil engineering structure such as the Poyang Lake Bridge, in order to perform its fatigue life estimation precisely, it is necessary to not only analyse the full bridge structure but also to obtain the accurate stress distributions locally. The approach where the full structure is simulated by a fine solid model would result in unreasonable calculating costs and low numerical efficiency. Thus, herein a hybrid scale approach with a coarse FE model for the full bridge and a fine solid model for its joints are established through the sub-model technique. For this variant, it takes nearly 20 hours to obtain final results for one configuration, on a PC with WINDOWS 7 operating system, I7 CPU, 16 GB RAM memory, and 2TB high-speed SATA hard disk, However, if the full bridge is fully modeled by a solid element model, this will result in hundreds of millions degrees-of-freedom, that any typical home/office PC could not cope with. Fig.6 shows a schematic diagram of the applied sub-model method philosophy. The welded thin steel plate of the steel bridge is simplified as shell elements, and the ANSYS Shell63 unit is employed to set up the full-bridge model. This results in a total of 106137 units that are meshed by using the quadrilateral element. Furthermore, the corresponding thermal and mechanical analysis FE models of the joint are using the ANSYS Solid 70 and Solid185 units respectively, and are meshed by using the high precision hexahedral elements, resulting in a total of 28834 meshed elements for the one critical joint. The cross section of the solid model is consistent with the design drawings of the steel bridge; those member bars connected with bolts are simplified into rigid connection bars. In addition, in order to precisely analyse the welding residual stress, the welded area of the box girder is divided in more scrutiny.

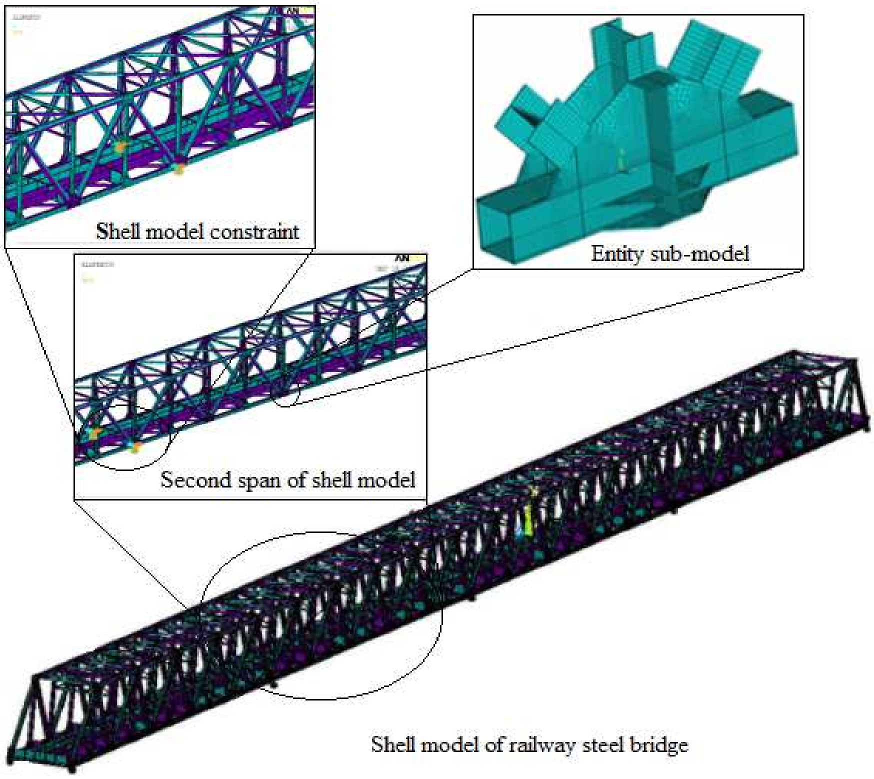

Fig. 6 Schematic diagram of railway steel bridge modelling based on sub-model method

4.3 Load simulation

4.3.1 Welding residual stresses

The FE simulation of the welding temperature field is using the double-ellipsoid heat source (Fig.7) to establish the welding heat source effect. The welding parameters are same as the actual arc welding parameters during construction. These are shown in Tab.1 [37]:

Tab.1 Welding parameters of electric arc welding

f_f	f_r	U_w (V)	I_w (A)	v (mm/s)	η (%)	a_1 (mm)	a_2 (mm)	b (mm)	c (mm)
1.33	0.67	270 V	10 A	6	70	5	10	3.5	5.0

The whole welding process is divided into the two stages, heating and cooling, and it is carried out with the same speed of 6 mm/s as in the actual construction. There are four welds in the box girder of the node, and the length of each weld is 4 m. The welding simulation is carried out in the same manner as with the factory process; the heating time is 1720 s, the cooling time is 1500 s, and the total welding time is 3220 s. Fig.8 shows the results of the temperature field on the joint at a given time. It can be seen from the chart that the heat gradually moves along with time, and that the welding temperature field distribution is non-uniform; the maximum temperature the heat source reaches is 1829 ˚C, which is realistic representation of the actual welding temperature [38]; the temperature decreases rapidly when the heat source passes through. Moreover, the isotherm near the heat source is as prescribed close to an ellipse.

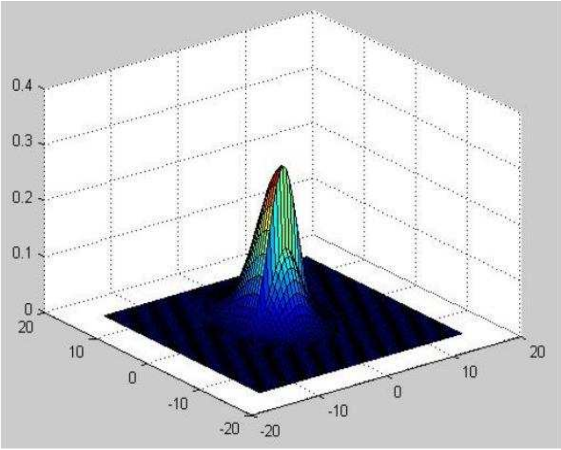

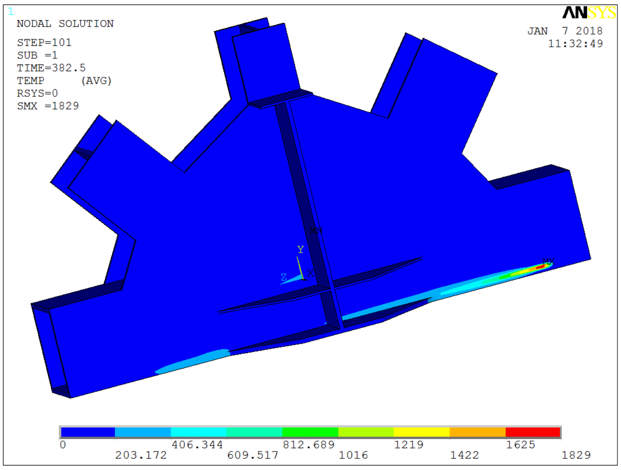

Fig.7 Double-ellipsoid heat source model **Fig.8 Temperature distribution of nodes**

Fig.9 shows the temperature time-history curve of the four different points in the welded area of the steel bridge joint during the welding process. It can be seen from the chart that in the heating stage, the weld area temperature rises sharply at the welding instant, and the temperature reaches its maximum value of around 1800 ˚C; in the cooling stage, the temperature drops rapidly, and asymptotically tends to the room temperature.

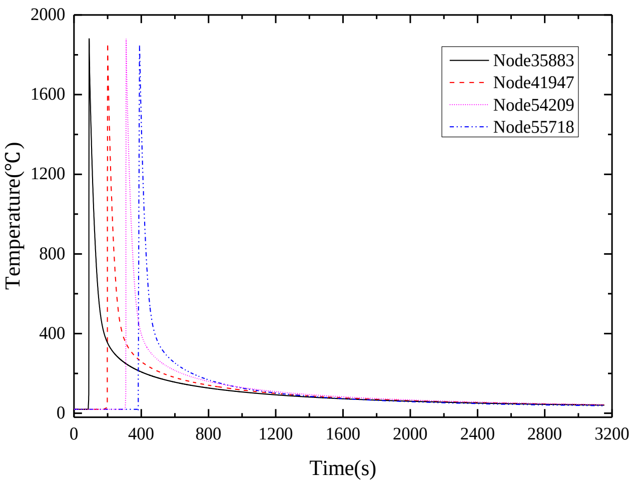

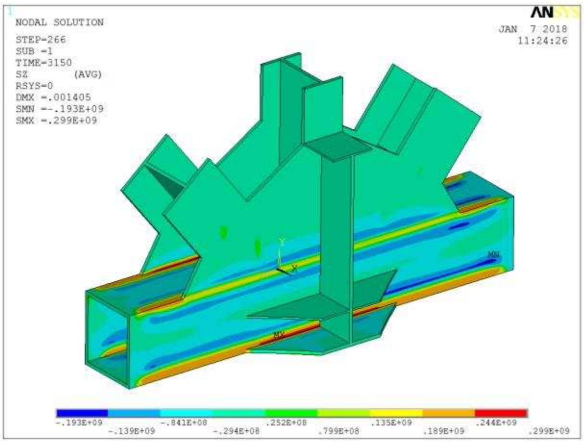

Fig. 9 Temperature time-history curve **Fig. 10 Nephogram of welded residual stress**

The residual stress field is analysed after the recovery of the temperature field. The temperature field is applied as the load to the fine stress analysis numerical model, and the simulation of welding residual stresses is achieved. In addition, the time course of the stress field analysis of the welding residual calculation is the same as that of the temperature field analysis. Fig.10 shows the nephogram of the welding residual stress, and as it can be seen from the chart these stresses are mainly distributed in the welds and their close vicinity. The welding residual stresses are tensile stresses, with a maximum value here of around 299 MPa. The location of the maximum welding residual stress is at the weld seam which connects the box girder and the node plate.

4.3.2 Train traffic load

According to the actual structure’s engineering background, the Tong-Jiu line is a freight route. With an average of six trains per hour crossing the Poyang Lake Bridge, the speed of the characteristic train is 72 km/h. For all simulations, the interval time was selected as 0.02 s, making the total time for a train passing through the bridge 38.32 s. Reviewing actual information on realistic train traffic over the bridge, an indicative train formation with a DF4 locomotive and thirty C62 carriages was selected. For more details on the specific train grouping parameters one can refer to the Yang et al. [39]; Fig.11 shows the schematic diagram of the train formation.

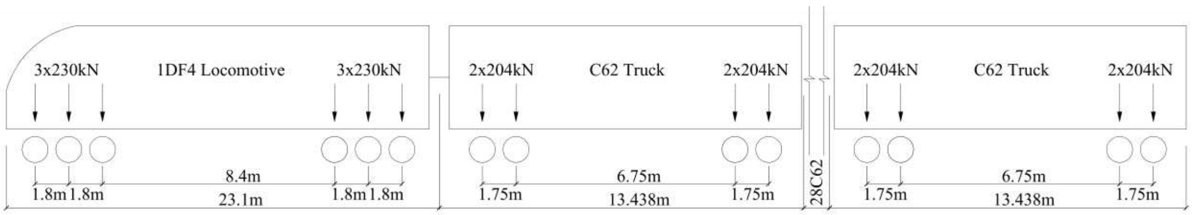

Fig.11 Schematic diagram of the train formation

The track parameters are shown in Tab.2, and the average interval between adjacent track nodes are nearly 1.15 m; this is actually also the distance considered between nodes in the full bridge shell model.

Tab.2 Track Parameters

Parameters	k_{y1} (MN/m)	k_{y2} (MN/m)	k_{y3} (MN/m)	c_{y1} (kN·s /m)	c_{y2} (kN·s /m)	c_{y3} (kN·s /m)	k_H (MN/m)
Value	3.92	220	133	63	82	100	150

The power spectrum of Germany high interference track irregularity is used to simulate the train traffic loads due to its suitability for the freight trains in China. Tab.3 gives the track irregularity parameters herein used.

Tab.3 Track irregularity parameters

A_v（m^2×rad/m）	Ω_c（rad/m）	Ω_r（rad/m）
1.08×10^{-7}	0.8246	0.0206

The time-history curve of the vertical track irregularity is simulated by using a FORTRAN-coded program based on the triangular series superposition method [30]. Results can be shown in Fig.12. The load time-history curve acting on the nodes of the full bridge shell FE model is obtained through the vehicle-track coupling dynamic model developed. Fig.13 shows the case of the load time-history curve for the later considered critical node in the middle span.

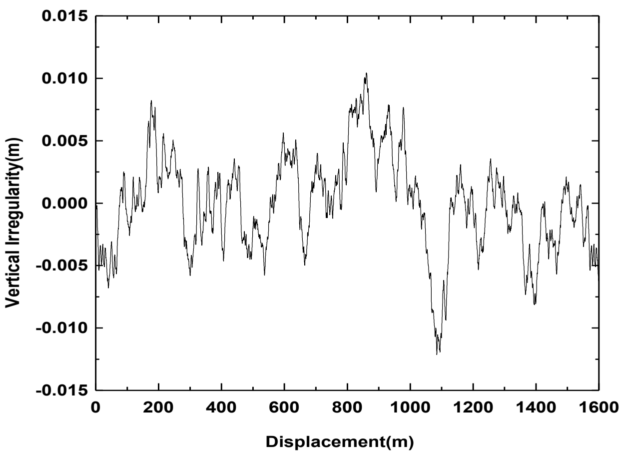

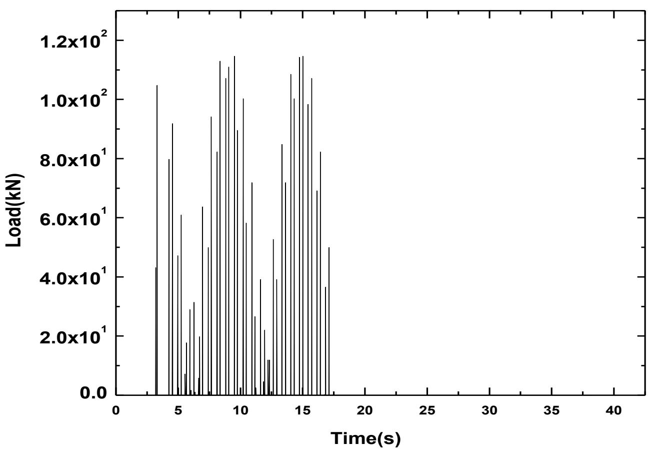

Fig.12 Time-history curve of vertical track irregularity **Fig.13 Time-history curve of load**

4.4 Joint dynamic response; the vibration control scenario

4.4.1 Detailing of the MR-TMD control system

Owing to the large vertical displacement response in the middle span of the railway bridge, the MR-TMD control system application is considered there, in order to obtain the best control performance effect against the train traffic load and without aesthetically affecting the bridge shape. To ensure that the MR-TMD installation does not affect the bridge shape and the trains passing over the bridge, we use 20 mass damper units which are distributed uniformly along the middle span. Fig.14 presents the layout of the MR-TMD control system set on one of the spans of the actual bridge. Tab.4 gives the basic modelling parameters of the MR-TMD system. Additionally, for the passive TMD part the stiffness is 750kN/m, and the inherent damping is 1.2kNs/m.

Tab.4 Parameters of each MR-TMD control system

Mass block (kg)	Maximum force (KN)	MR diameter of cylinder (mm)	MR diameter of piston shaft (mm)	Effective length of piston (mm)
1200	100	140	70	120

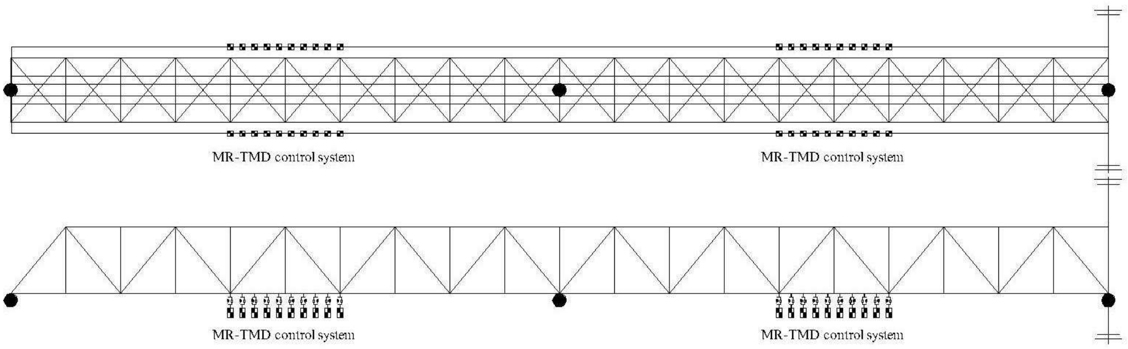

Fig.14 Layout of the MR-TMD control system in one of span of bridge; top: Front view; bottom: Side view

4.4.2 Stress evaluation for the critical joint location

As discussed earlier, the accurate stress response on any joint of the railway bridge is obtained based on a sub-model realisation. Fig.15 gives the time-history of the vertical displacement at one node on the solid model boundary of the original structure from both the FORTRAN and ANSYS models. As it can be seen, the amplitude of the vertical displacement extracted in both cases are identical at 0.0326 m. Therefore, both models are consistent, giving an amplitude for vertical displacement that makes the fatigue damage easy to occur under the long time high frequency train traffic.

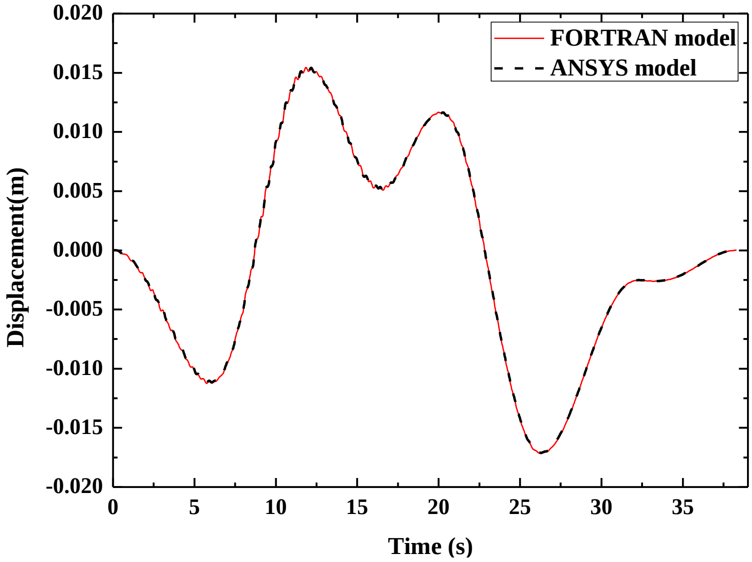

Fig.15 Time-history curve of vertical displacement

Fig.16 shows the Von-Mises stress contours after analysis of the original structure. What it shows is that the position connecting the edge of the gusset plate and the box girder has the largest welding stress and this is likely to produce stress concentration that could subsequently instigate the fatigue process. Therefore, this position is regarded as the most dangerous point to determine the fatigue crack initial life of the whole railway bridge and this is considered the same for all relevant later calculations.

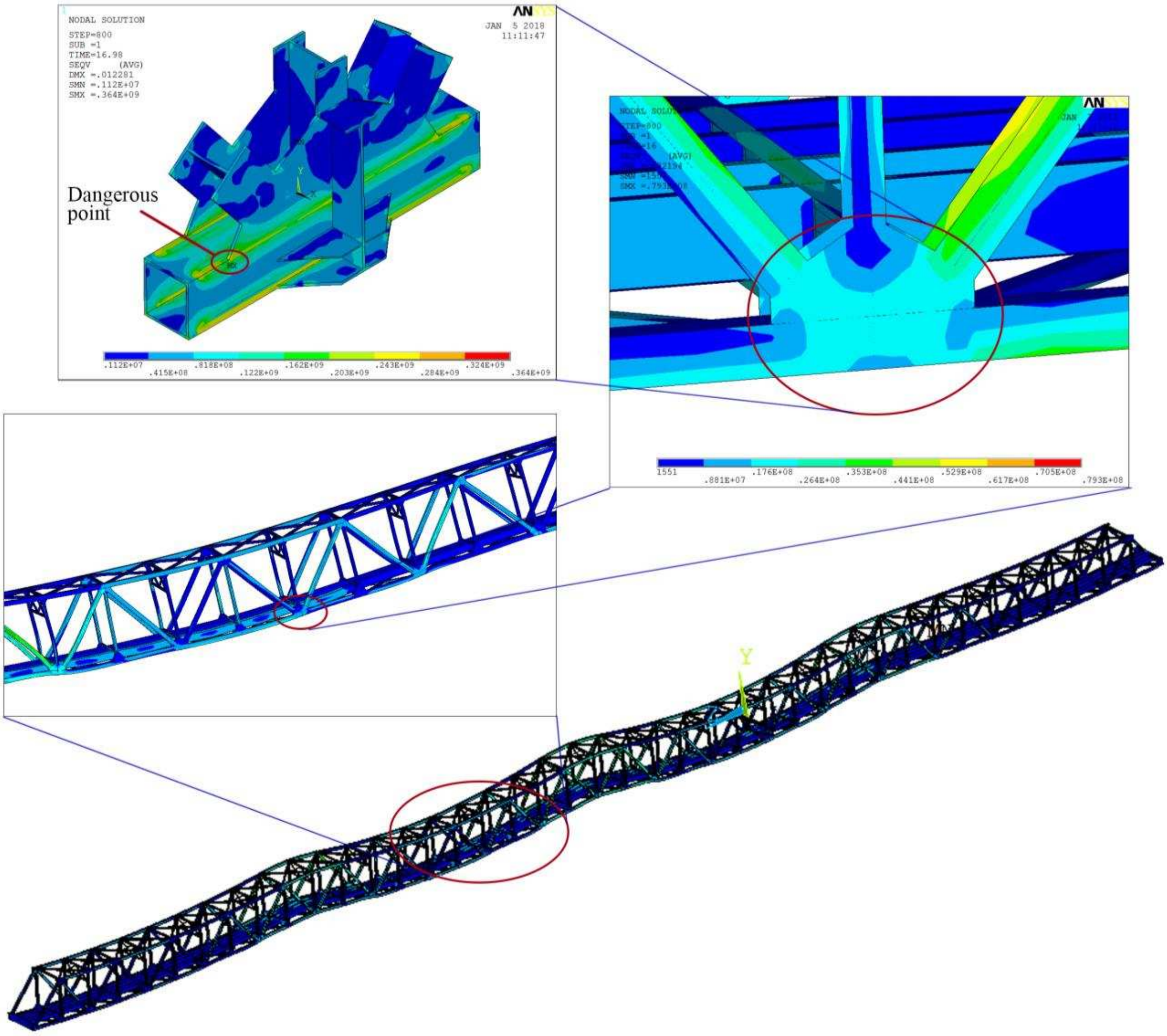

Fig.16 Von-Mises stress contour of the bridge

Fig.17 presents the vertical normal strain time-history curve locally at the dangerous point. The maximum value of the normal strain is 560×10^{-6}, and this is the variable that gets the most influence on fatigue. The contribution of the vibration control method could impact on this and reduce it in a way that substantially prolongs the time to initiate any fatigue cracking condition.

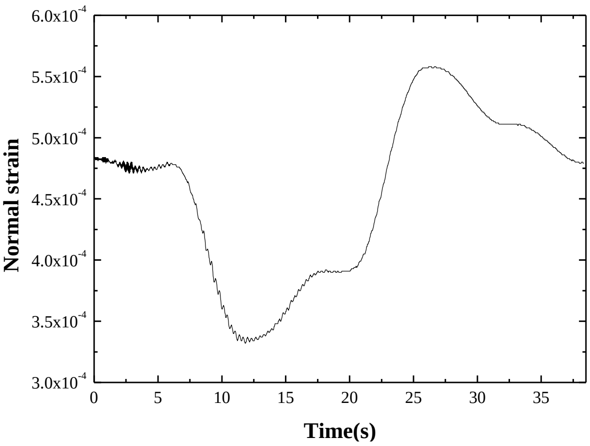

Fig.17 Vertical normal strain time-history curve

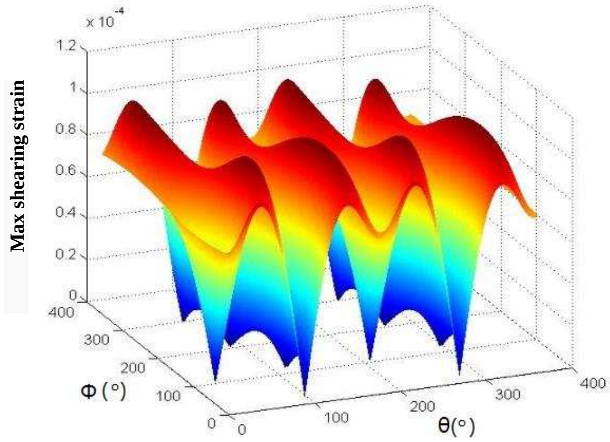

Fig.18 Search results of critical damage plane

Due to the welded joints of the steel bridge being in a multi-axial stress state, it is necessary to determine the critical plane of the dangerous point for the fatigue life assessment based on the fatigue damage critical plane method. Using the six components of the strain time-history curves, at the point level as obtained in the previous section, the position of the maximum shear strain plane derived parameter space at a given time is shown in the Fig.18. The orientation of the critical plane calculated by the weight function method, for the illustration in hand, is $[\theta', \Phi'] = [262°, 181°]$.

4.4.3 Dynamic stress response under various control scenarios

In order to analyse the effect of different control solutions on extending the fatigue crack initiation life, first the dynamic response for the critical plane of the considered point under the different control scenarios is obtained. The MR-TMD intelligent control system, with the fixed increment algorithm prescribed, is used as the base towards accomplishing the vibration reduction objective for the bridge response. For this, the fixed increment adjustment value is set at 20% of the maximum current. At the same time, in order to research the effect of the control algorithm in the MR-TMD system, two relevant uncontrolled cases were considered where the current was set constant to the minimum and maximum values; these correspond to the MR damper being fully closed or fully opened respectively. Subsequently, a designated state of passive-off control is considered when functioning constantly at minimum current, while a passive-on control is considered when functioning repeatedly at the maximum current.

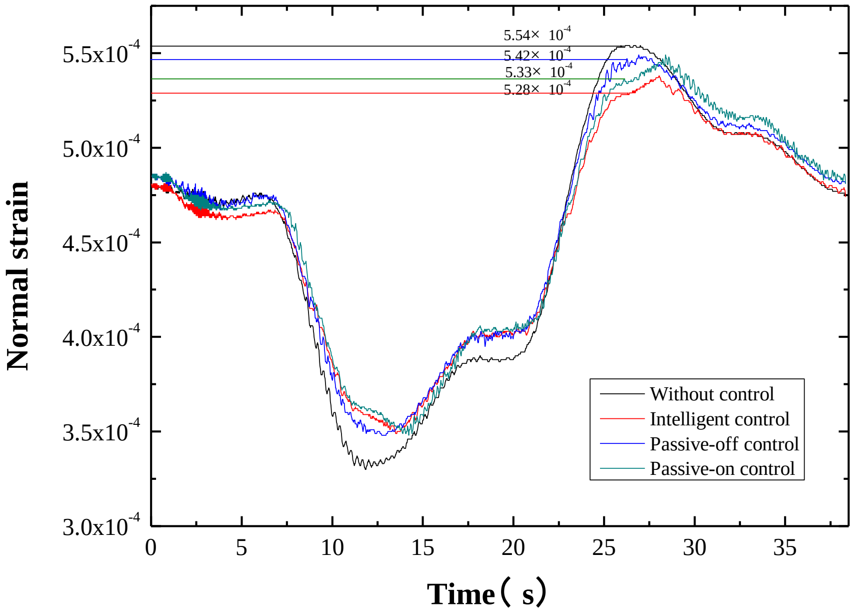

(a) Normal strain time-history curve

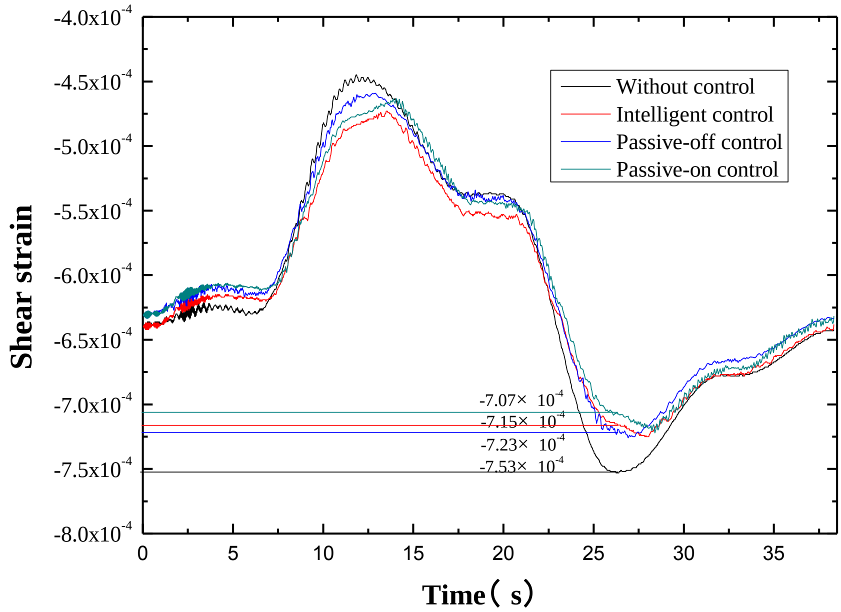

(b) Shear strain time-history curve

Fig.19 The effect of different control option on strain

Fig.19 shows the normal and shear strain time-history curves for the structure with passive-off, passive-on, intelligent control and without control when the freight train at 72 km/h speed passes through the railway bridge. It can be seen that, at the time 25.94 s, the normal strain of the structure with passive-off, passive-on, intelligent control and without control are 5.42×10^{-4}, 5.33×10^{-4},

5.28×10^{-4}, and 5.54×10^{-4} respectively. Similarly, at the time 26.24 s, the shear strain of the structure with passive-off, passive-on, intelligent control and without control, are (in absolute values) 7.23×10^{-4}, 7.07×10^{-4}, 7.15×10^{-4}, and 7.53×10^{-4} respectively. It is observed that the bridge with all control variants can show good control performance, giving evidence of potential for extending the fatigue crack initiation life of the bridge. The control effect of the passive-on control is at instants better than the intelligent control in terms of shear strain. However, holistically, the normal strain with intelligent control is better than when with passive-on control, which also affects the fatigue life through an equivalent strain measure.

Although these absolute strain values reduced only slightly there is a more significant effect on amplitudes, on which the fatigue life directly depends on. Thus, it is also necessary to calculate the strain cycle amplitude to judge the merits of the control effect.

4.5 Sizing the extension of fatigue crack initiation life for the railway bridge

4.5.1 Calculation and analysis of equivalent damage parameter

The normal strain and shear strain time-histories are accounted for by the rain-flow counting method. The amplitude and frequency of each cycle are extracted as shown in the Fig.20. It can be seen that the intelligent control has the best control effect among all different considered scenarios.

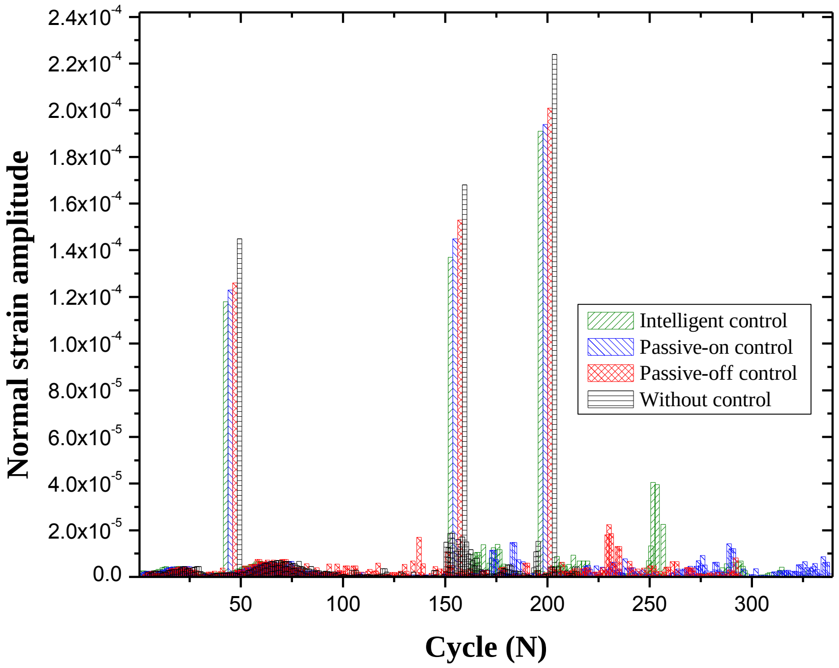

(a) Diagram of normal strain amplitude

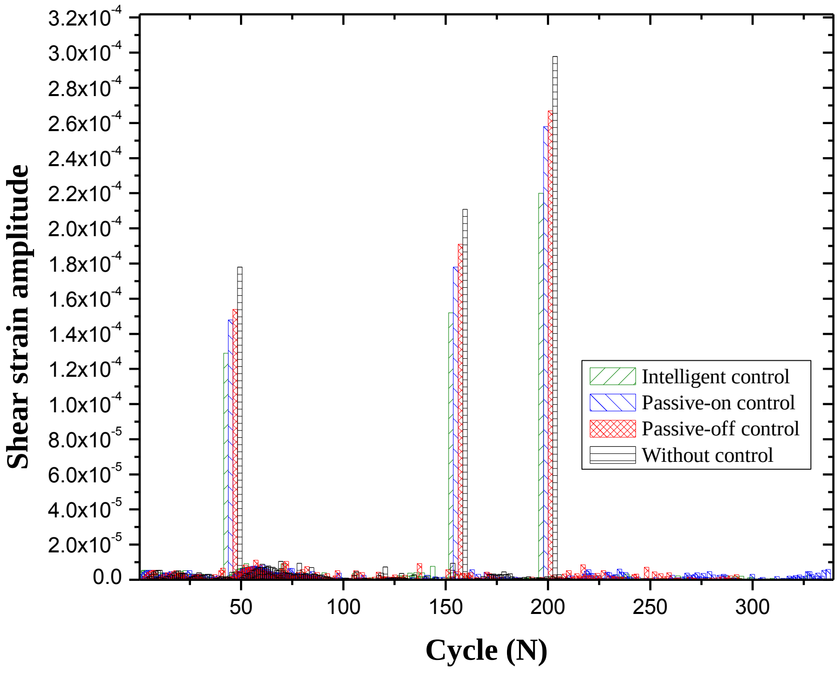

(b) Diagram of shear strain amplitude

Fig.20 Diagram of normal and shear strain amplitude

According to Eq.6, the parameters of the normal and shear strain amplitudes on the critical plane are synthesized to the equivalent strain amplitude, and this is used as the damage control parameter. Fig.21 gives these equivalent strain amplitudes. It is shown that the maximum equivalent strain amplitude of the structure without control is 4.80×10^{-4}, while for the passive-off, passive-on and intelligent control are 4.30×10^{-4}, 4.16×10^{-4} and 4.02×10^{-4}, respectively. This means that the maximum equivalent strain amplitude is reduced by 10.4%, 13.3% and 16.3% when compared to the original status. In addition, the rain-flow counting number of the original structure with passive-off, passive-on, intelligent control and without control are 293, 339, 333 and 211 respectively. Although, there are differences in the number of cycles, the fatigue damage of the joint is produced only by the three larger strain amplitudes and all other cycles were found too small to cause any substantial damage. Thus, there is an evident control effect of the MR-TMD at all the aspects that affect the fatigue life later calculations.

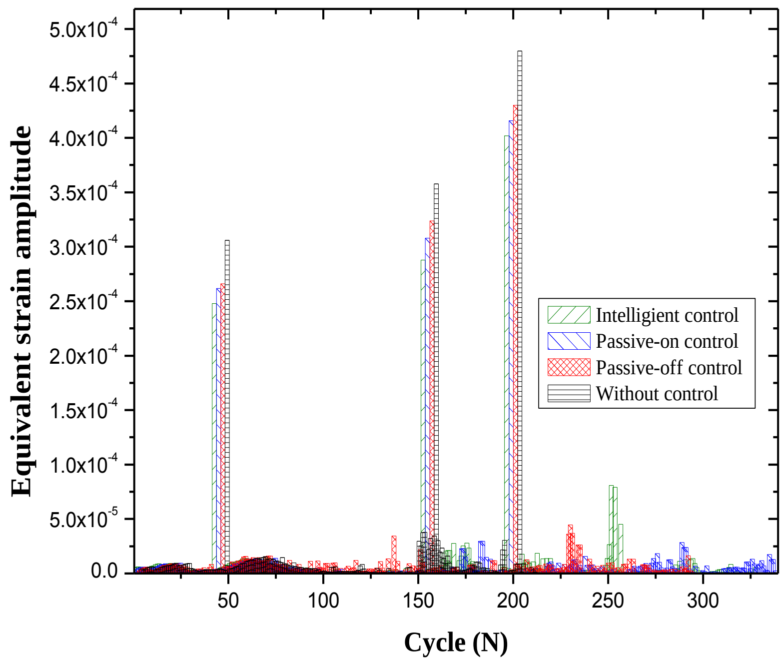

Fig.21 Diagram of equivalent strain amplitude

4.5.2 Estimation of fatigue crack initial life

Finally, the Manson-Conffin formula of Eq.(25) is used in order to assess the fatigue crack initiation life of the bridge. For the basic involved parameters it was considered that $\sigma_f^{'}-\sigma_m$=554 MPa, b=-0.1632, c=-0.6824, $\varepsilon_f^{'}$=1.0118 [40].

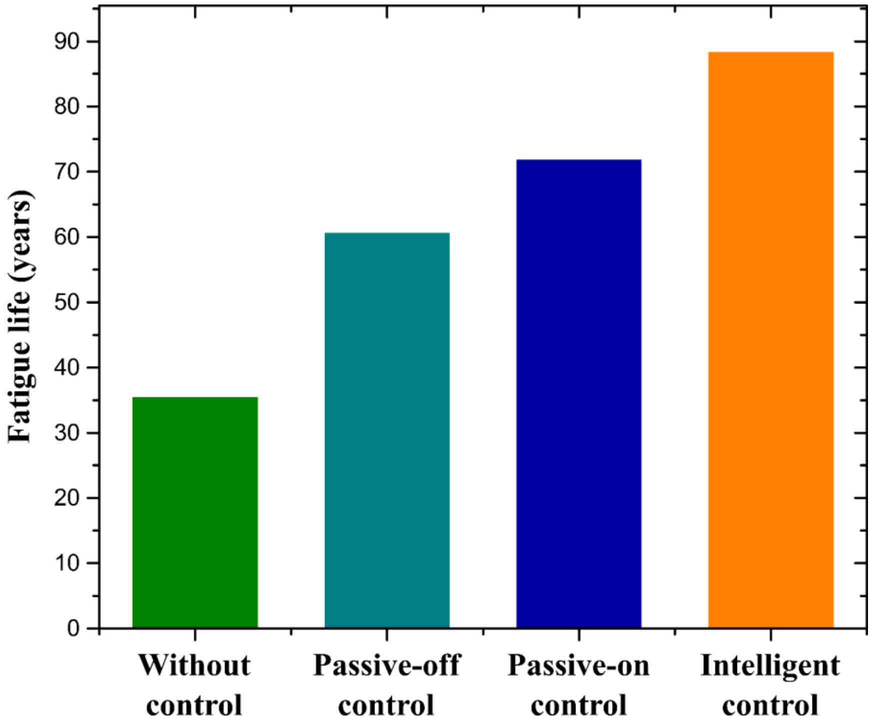

Fig.22 Comparison of fatigue life with various control

According to the Miner's linear fatigue cumulative damage criterion mentioned in section 3.4, using the equivalent strain amplitude, the fatigue damage degree of the railway steel bridge without control is 5.367×10^{-7}, and the relevant number of cycles is 1863200. Similarly, the fatigue damage degree of the bridge structure with passive-off, passive-on and intelligent control are 3.137×10^{-7}, 2.648×10^{-7} and 2.153×10^{-7}, respectively while the associated number of cycles are 3187800, 3776400 and 4645300. According to the actual structural engineering details, the fatigue crack initiation life of the bridge is obtained as shown in the Fig.22. As it can be seen that the fatigue crack resistance of the bridge in-hand has improved to a high degree with all the various control options. Among them, the intelligent control solution brings the best results, whereby it raised the structural life estimate to 88.38 years, giving a relative increase, compared to the original structure, of the order of 150%.

5. Conclusions

This paper presented an analytical framework for sizing the fatigue life extension of railway steel bridges when dynamically controlling their response. The tested of a real case bridge was employed for showcasing the effectiveness and merit of the endeavour. The main outputs derived include

(1) The multi-scale analysis method devised for establishing the railway steel bridge model not only meets the need of evaluating accuracy for the stress concentrations at the welded joints, but also has high computational efficiency

(2) The MR-TMD intelligent control system proposed even when using an easy-to-implement fixed increment algorithm can effectively control both the normal and shear strain amplitudes at the fatigue-dangerous bridge point, reducing the equivalent strain amplitude to be used in fatigue modelling.

(3) The degree of fatigue damage of the Poyang Lake railway steel bridges when using an MR-TMD intelligent control system and under the combined realistic effect of train traffic load and welding residual stress is 2.153×10^{-7}, the relevant number of cycles is 4645300, and the calculated fatigue life 88.38 years. Compared to the original structure without any control this means an increase by almost 150%. Therefore, the control effect of the MR-TMD control system makes it a well-substantiated structural solution.

Acknowledgments

The authors gratefully acknowledge the support for this research by the National Natural Science Foundation of China under Grant Nos. (51108363 and 51478372), Hubei Key Laboratory of Roadway Bridge and Structure Engineering (Wuhan University of Technology) (No.DQJJ201707) and Natural Science Foundation of Hubei Province (No. 2016CFA020).

Reference

[1] Committee on Fatigue and Fracture Reliability of the Committee on Structural Safety and Reliability of the Structural Division. Fatigue reliability: Parts 1–4. Journal of Structural Division, ASCE, 1982, **108**(ST1):3-88.

[2] Hansen B. Bridge Collapse Prompts Investigation, Raises Questions. Civil Engineering, ASCE, 2007, **77**(9):12-14.

[3] Fisher JW. Fatigue and Fracture of Steel Bridges: Case Studies. Willey-Interscience, 1984.

[4] Chryssanthopoulos MK, and Righiniotis TD. Fatigue reliability of welded steel structures. Journal of Constructional Steel Research. 2006, **62**(11):1199-1209.

[5] Shang D, and Wang D. Multi axis fatigue strength. Beijing: Science Press. 2007. (in Chinese)

[6] Li ZX, Chan THT, and Ko JM. Fatigue damage model for bridge under traffic loading: application made to Tsing Ma Bridge. Theoretical and Applied Fracture Mechanics, 2001, **35**(1):81-91.

[7] Xu YL, Liu TT, and Zhang WS. Buffeting-induced fatigue damage assessment of a long suspension bridge. International Journal of Fatigue, 2009, **31**(3):575-586.

[8] Guo T, Li AQ, and Wang H. Influence of ambient temperature on the fatigue damage of welded bridge decks. International Journal of Fatigue, 2008, **30**(6):1092-1102.

[9] Righiniotis TD. Effects of increasing traffic loads on the fatigue reliability of a typical welded bridge detail. International Journal of Fatigue, 2006, **28**(8):873-880.

[10] Tubino G, and Piccardo G. Tuned Mass Damper optimization for the mitigation of human-induced vibrations of pedestrian bridges. Meccanica, 2015, **50**(3):809-824.

[11] Yang GQ. Large-scale magneto-rheological fluid damper for vibration mitigation: Modeling, testing and control. PhD Dissertation University of Notre Dame, Indiana, USA. 2001.

[12] Fujino Y. Vibration, control and monitoring of long-span bridges-recent research, developments and practice

in Japan. Journal of Constructional Steel Research, 2002, **58**(1):71-97.

[13] Caetano E, Cunha Á, Magalhães F, and Moutinho C. Studies for controlling human-induced vibration of the Pedro e Inês footbridge: Part 2. Engineering Structures, 2010, **32**(4):1082-1091.

[14] Andersson A, O'Connor A, and Karoumi R. Passive and Adaptive Damping Systems for Vibration Mitigation and Increased Fatigue Service Life of a Tied Arch Railway Bridge. Computer-Aided Civil and Infrastructure Engineering, 2015, **30**(9):748-757.

[15] Museros P, and Martinez-Rodrigo MD. Vibration control of simply supported beams under moving loads using fluid viscous dampers. Journal of Sound and Vibration, 2007, **300**(1-2):292-315.

[16] Martínez-Rodrigo MD, Lavado J, and Museros P. Dynamic performance of existing high-speed railway bridges under resonant conditions retrofitted with fluid viscous dampers. Engineering Structures, 2010, **32**(4):808-828.

[17] Wang H, Tao T, Cheng H, and He X. Simulation Study on Train-Induced Vibration Control of a Long-Span Steel Truss Girder Bridge by Tuned Mass Dampers. Mathematical Problems in Engineering, 2014, (2014), 506578:1-12.

[18] Luu M, Zabel V, and Könke C. An optimization method of multi-resonant response of high-speed train bridges using TMDs. Finite Elements in Analysis and Design, 2012, **53**(6):13-23.

[19] Younesian D, Kargarnovin MH, and Esmailzadeh E. Optimal passive vibration control of Timoshenko beams with arbitrary boundary conditions traversed by moving loads. Proceedings of the IMechE, Part K: Journal of Multi-body Dynamics, 2008, **222**(2):179-188.

[20] Kahya V, and Araz O. Series tuned mass dampers in train-induced vibration control of railway bridges. Structural engineering and mechanics, 2017, **61**(4):453-461.

[21] Yau JD. Train-Induced Vibration Control of Simple Beams Using String-Type Tuned Mass Dampers. Journal of Mechanics, 2007, **23**(4):329-340.

[22] Lin CC, Wang JF, and Chen BL. Train-Induced Vibration Control of High-Speed Railway Bridges Equipped with Multiple Tuned Mass Dampers. Journal of Bridge Engineering, 2005, **10**(4):398-414.

[23] Fu G, Gu J, Lourenco MI, Duan M, and Estefen SF. Parameter determination of double-ellipsoidal heat source model and its application in the multi-pass welding process. Ships and Offshore Structures, 2014, **10**(2):204-217.

[24] Zhao Q, Guo Z, Shen X, and Briseghella B. Test study on residual stress distribution of hybrid steel u-rib stiffened plates. Journal of Constructional Steel Research, 2016, **121**:261-267.

[25] Armentani E, Pozzi A, and Sepe R. Finite-element simulation of temperature fields and residual stresses in butt welded joints and comparison with experimental measurements, In: Proceedings of 12th Biennial ASME Conference on Engineering Systems Design and Analysis (ESDA2014), Copenhagen, Denmark, 2014, pp. V001T04A005.

[26] Cho DW, Song WH, Cho MH, and Na SJ. Analysis of submerged arc welding process by three-dimensional computational fluid dynamics simulations. Journal of Materials Processing Technology, 2013, **213**(12):2278-2291.

[27] Perić M, Tonković Z, Rodić A, Surjak M, Garašić I, Boras I, and Švaić S. Numerical analysis and experimental investigation of welding residual stresses and distortions in a T-joint fillet weld. Materials and Design, 2014, **53**:1052-1063.

[28] Xia H. Vibration Engineering of Traffic Environment. Beijing: Science Press. 2010. (in Chinese)

[29] Lei X. New methods of orbital mechanics and Engineering. Beijing: China Railway Press. 2002. (in Chinese)

[30] Wang Y, Li Z, Wang C, and Wang H. Concurrent multi-scale modelling and updating of long-span bridges using a multi-objective optimisation technique. Structure and Infrastructure Engineering, 2013, **9**(12):1251-1266.

[31] Liljedahl CDM, Zanellato O, Fitzpatrick ME, Lin J, and Edwards L. The effect of weld residual stresses and their re-distribution with crack growth during fatigue under constant amplitude loading. International Journal of Fatigue, 2010, **32**(4):735-743.

[32] Qu WL, Qin SQ, Tu JW, Liu J, Zhou Q, Cheng H, and Pi YL. Intelligent control for braking-induced longitudinal vibration responses of floating-type railway bridges. Smart Materials and Structures, 2009, **18**(12), 125003.

[33] Brighenti R, Carpinteri A, Macha E, and Spagnoli A. Weight function method for determination of critical plane position under multiaxial loading. In: 12^{th} European Conference of Fracture (EFC12), Fracture from Defects, Sheffield, UK, 1998, pp. 205-210.

[34] Ligaj B, and Szala G. Comparative analysis of fatigue life calculation methods of C45 steel in conditions of variable amplitude loads in the low- and high-cycle fatigue ranges. Polish Maritime Research, 2012, **19**(4):23-30.

[35] Shen W, Yan R, Xu L, Zhang X, and Geng L. Study on multi-axial fatigue damage of weld joints considering residual stress. Ship building of China, 2014, **55**(2):67-76.

[36] Kim HI, Huh Y, and Seok CS. Fatigue Life Evaluation of an Actual Structure under the Irregular Loading Using an Acceleration Test. Solid State Phenomena, 2007, **120**:9-14.

[37] ANSI/AASHTO/AWS D1.5M/D 1.5:2010. Bridge Welding Code.

[38] Liang W, Murakawa H, and Deng D. Investigation of welding residual stress distribution in a thick-plate joint with an emphasis on the features near weld end-start. Materials and Design, 2015, **67**(67):303-312.

[39] Yang YB, Yau JD, and Wu YS. Vehicle-Bridge Interaction Dynamics: With Applications to High-Speed Railways. World Scientific, 2004.

[40] Chen X, and Huang D. Low cycle fatigue of 14MnNbq steel welded joints. Journal of Tianjin University, 2001, 34(3):386-388. (in Chinese)